

A Comparative Study on Shadow Compensation of Color Aerial Images in Invariant Color Models

Victor J. D. Tsai

Abstract—In urban color aerial images, shadows cast by cultural features may cause false color tone, loss of feature information, shape distortion of objects, and failure of conjugate image matching within the shadow area. This paper presents an automatic property-based approach for the detection and compensation of shadow regions with shape information preserved in complex urban color aerial images for solving problems caused by cast shadows in digital image mapping. The technique is applied in several invariant color spaces that decouple luminance and chromaticity, including HSI, HSV, HCV, YIQ, and YC_bC_r models. Experimental results from de-shadowing color aerial images of a complex building and a highway segment in these color models are evaluated in terms of visual comparisons and shadow detection accuracy assessments. The results show the effectiveness of the proposed approach in revealing details under shadows and the suitability of these color models in de-shadowing urban color aerial images.

Index Terms—Color model, de-shadowing, shadow compensation, shadow detection, thresholding.

I. INTRODUCTION

IN urban aerial images, shadows are usually cast by elevated objects such as various cultural features (buildings, bridges, towers, etc.) when they are illuminated by the Sun at the time of exposures. Shadow can provide additional geometric and semantic clues about the shape and position of its casting object and the position of the light source [1]–[3]. On the other hand, objects within shadows reflect little radiance and require much attention to discern on aerial images because the incident illumination is occluded by the casting objects. As a result, cast shadows may cause loss of feature information, false color tone, shape distortion of objects, and failure of conjugate image matching within the shadow area. Hence, effects caused by cast shadows in color aerial images of complex urban environment demand solutions for digital image mapping.

Though there were several techniques in the literature in detecting shadows in black and white (B&W) aerial images [4]–[10], relatively limited work has been found for identifying and correcting shadows in color aerial images in which radiometric reflections from features in the scene are recorded in color tones. Considering the atmospheric Rayleigh scattering effect, Polidoro *et al.* [2] proposed a robust technique to segment shaded areas in color images obtained by airborne and orbital sensors by simply thresholding the difference image of the saturation and the intensity components for each pixel in

a normalized hue, saturation, and intensity (HSI) color space. Susuki *et al.* [11] presented a method that applies separation of spatial frequency components and probabilistic shadow segmentation in the red, green, and blue (RGB) space and compensations of intensity and saturation values to improve the visibility of features in shadowed regions while retaining nonshadowed regions and the natural tint of shadowed regions. Recently, Huang *et al.* [12] presented an imaging model of shadows based on Phong illumination model [13] and employed thresholding on the *hue*, *blue*, and *green-blue* difference components sequentially to detect shadowed areas, which were then compensated by applying the Retinex technique to both shadowed and nonshadowed areas separately.

However, automation on shadow compensation in these efforts is not accomplished due to the following drawbacks [11]–[13].

- 1) Image and scene analysis is required for determining optimal thresholds to identify shadows cast by various features in different surrounding environments.
- 2) Intensive calculation of the Bayesian likelihood *a posteriori* probabilities in the RGB space, as well as the determination of several heuristic coefficients for intensity and saturation compensations, are demanded.
- 3) Attention is also required on determining the thresholds to carefully exclude both bluish and greenish objects from the shadow segments.

This paper presents an automatic property-based de-shadowing approach for solving the problems caused by cast shadows in color aerial images of complex urban environment. The proposed approach exploits the properties of shadows in luminance and chromaticity and is applied in several invariant color spaces, including HSI; hue, saturation, and value (HSV); hue, chroma, and value (HCV), luma, inphase, and quadrature (YIQ); and YC_bC_r models. Experimental results from applying the proposed approach in de-shadowing two color aerial images of a complex building and a highway segment in these color models are evaluated in terms of visual comparisons and shadow detection accuracy assessment. The results demonstrate the effectiveness of the proposed approach in revealing details under shadows and the suitability of these color models in de-shadowing color aerial images.

II. PHOTOMETRIC INVARIANT COLOR MODELS

In color aerial images, color tone is a powerful descriptor that simplifies and dominates feature identification and extraction in visual interpretation applications. Basically, the color that human beings perceive in an object is determined by the quality

Manuscript received January 26, 2005; revised December 12, 2005.

The author is with the Department of Civil Engineering, National Chung Hsing University, Taichung 402, Taiwan, R.O.C. (e-mail: jdtsai@nchu.edu.tw).
Digital Object Identifier 10.1109/TGRS.2006.869980

of a chromatic light source in three quantities: *radiance*, *luminance*, and *brightness* [14]. Objects in an aerial scene reflect the chromatic electro-magnetic radiance (EMR) emitted from the Sun and show various colors subjective to their reflectance to the three primary wavelengths in *red* (R), *green* (G), and *blue* (B) as designated by the Commission Internationale de l'Eclairage (CIE). Thus, all colors are seen as variable combination of the three primaries in the RGB color model, which is usually used in representing and displaying images. Besides, several color models that decouple *luminance* and *chromaticity* are briefly described in the following in terms of their relations with the RGB model.

A. HSI Model

The HSI model [15] manipulates color images with the following transformation from the RGB model:

$$\begin{bmatrix} I \\ V_1 \\ V_2 \end{bmatrix} = \begin{bmatrix} \frac{1}{3} & \frac{1}{3} & \frac{1}{3} \\ -\frac{\sqrt{6}}{6} & -\frac{\sqrt{6}}{6} & \frac{\sqrt{6}}{3} \\ \frac{1}{\sqrt{6}} & \frac{2}{\sqrt{6}} & 0 \end{bmatrix} \begin{bmatrix} R \\ G \\ B \end{bmatrix} \quad (1)$$

$$S = \sqrt{V_1^2 + V_2^2} \quad (2)$$

$$H = \tan^{-1} \left(\frac{V_2}{V_1} \right) \quad (3)$$

if $V_1 \neq 0$, otherwise H is undefined.

Note that *hue* and *saturation* taken together are called *chromaticity* and the *brightness* of a chromatic light embodies the achromatic notion of *intensity* [14].

B. HSV Model

Smith [16] described a triangle-based HSV model in the following relations with the RGB model:

$$V = \frac{1}{3}(R + G + B) \quad (4)$$

$$S = 1 - \frac{3}{R + G + B} \min(R, G, B) \quad (5)$$

$$H = \begin{cases} \theta & \text{if } B \leq G \\ 360^\circ - \theta & \text{if } B > G \end{cases} \quad (6)$$

in which

$$\theta = \cos^{-1} \left\{ \frac{\frac{1}{2}[(R - G) + (R - B)]}{\sqrt{(R - G)^2 + (R - B)(G - B)}} \right\}.$$

C. HCV Model

The HCV model [17] describes the dominant frequency, the amount of color, and luminance, respectively, in the following relations with the RGB model:

$$V = \frac{1}{3}(R + G + B) \quad (7)$$

$$H = \tan^{-1} \left[\frac{R - B}{\sqrt{3}(V - G)} \right] \quad (8)$$

$$C = \begin{cases} \frac{V - G}{\cos H}, & \text{if } |\cos H| > 0.2 \\ \frac{R - B}{\sqrt{3} \sin H}, & \text{if } |\cos H| \leq 0.2 \end{cases} \quad (9)$$

D. YIQ Model

The YIQ color model is a widely supported standard in National Television Standards Commission (NTSC) color

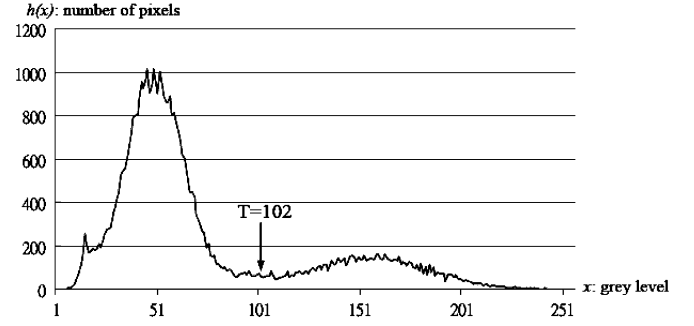


Fig. 1. Automatic threshold determination by applying Otsu's method.

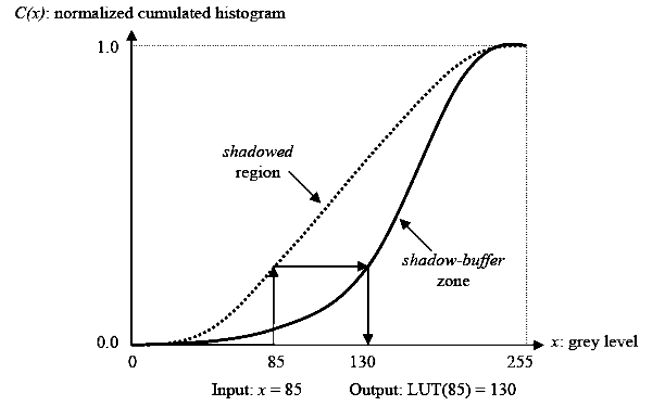


Fig. 2. Grey-level LUT generation in the histogram matching approach.

TV transmission. In this scheme, Y is proportional to the gamma-corrected *luminance*, which corresponds roughly with *intensity*, and I and Q jointly describe the *chroma*, which corresponds with *hue* and *saturation*, of a color image in the following relations with the RGB model [14], [15], [18]:

$$\begin{bmatrix} Y \\ I \\ Q \end{bmatrix} = \begin{bmatrix} 0.299 & 0.587 & 0.114 \\ 0.596 & -0.275 & -0.321 \\ 0.212 & -0.523 & 0.311 \end{bmatrix} \begin{bmatrix} R \\ G \\ B \end{bmatrix} \quad (10)$$

E. YC_bC_r Model

The YC_bC_r model is used in most video and image compression standards like JPEG, MPEG, and H2.63+ [19] for the transmission of *luma* and *chroma* components coded in the integer range [0, 255]. It has the following relations with the RGB model [20]:

$$\begin{bmatrix} Y \\ C_b \\ C_r \end{bmatrix} = \begin{bmatrix} 0.257 & 0.504 & 0.098 \\ -0.148 & -0.291 & 0.439 \\ 0.439 & -0.368 & -0.071 \end{bmatrix} \begin{bmatrix} R \\ G \\ B \end{bmatrix} + \begin{bmatrix} 16 \\ 128 \\ 128 \end{bmatrix} \quad (11)$$

Note that the V component in both HSV and HCV models as well as the Y component in the YIQ and YC_bC_r models are identical or equivalent to the I component in the HSI model. These components are then called *intensity-equivalent* (I_e) components. So are the Q component in the YIQ model and C_r component in the YC_bC_r model equivalent to the H component in the HSI model. These components are then called *hue-equivalent* (H_e) components. Both I_e and H_e components of the



Fig. 3. RGB color aerial images (Courtesy of Great Wing Airlines, Taiwan, R.O.C.). (a) A complex building. (b) A highway segment.



Fig. 4. Manually interpreted *shadow masks* (white area) as ground truth of shadow regions. (a) Shadow of the image in Fig. 3(a). (b) Shadow of the image in Fig. 3(b).

transformed images were used in the proposed de-shadowing approach described in the following.

III. PROPERTY-BASED DE-SHADOWING APPROACH

It is not difficult for human interpreters to identify shadows in color aerial images because shadow itself is one of the fundamental elements in visual photo interpretation [1], [3]. However, identifying shadows in color aerial images of complex urban scenes by computer programs involves developing algorithms for solving many difficult problems, including boundary ambiguity, color inconstancy, illumination variation, atmospheric effect, etc. The first step toward de-shadowing in color aerial images involves exploiting the luminance and chromaticity properties of shadows. It has been observed that shadowed regions in color aerial images hold the following properties:

- 1) lower luminance (intensity) because the EMR from the Sun is obstructed;
- 2) higher saturation with short *blue-violet* wavelength due to atmospheric Rayleigh scattering effect [2], [21];
- 3) increased hue values because the change of intensity of an area when shadowed and not shadowed is positive proportional to the wavelength [12].

These properties are easily discovered when the normalized photometric invariant color models mentioned above are used. Considering the above properties, the H_e and I_e components are used in the proposed approach which involves the following four steps.

A. Color Transformation

The RGB-based color aerial images are transformed into the photometric invariant color model under investigation using corresponding relations as described above. For comparison

purpose, transformed components in these color models are all scaled to the range of values in [0, 1] for shadow segmentation.

B. Shadow Segmentation

Both H_e and I_e components are considered in extracting the shadowed area in color aerial images. The *spectral ratioing* technique is applied to obtain the $(H_e + 1)/(I_e + 1)$ *ratio image*, which is scaled to have pixels' values in [0, 255]. The $(H_e + 1)/(I_e + 1)$ *ratio image* shall enhance the increased *hue* property of shadows with low luminance, i.e., pixels in shadowed regions will have higher values in the $(H_e + 1)/(I_e + 1)$ *ratio image* than those pixels in nonshadowed regions. The Otsu's method [22] is then applied over the histogram of the *ratio image* to automatically determine the threshold for segmenting the regions in shadow into a logical *shadow mask* for those pixels with value greater than the threshold. The Otsu's method finds an optimal threshold T , which maximizes [23]

$$V(T) = \frac{(\bar{\mu} \cdot w(T) - \mu(T))^2}{w(T) \cdot \mu(T)} \quad (12)$$

where $w(T) = \sum_{i=0}^T p_i$, $\mu(T) = \sum_{i=T+1}^{255} p_i$, $\bar{\mu} = \sum_{i=0}^{255} i \cdot p_i$, and p_i is the probability of pixels with grey level i in the image. For instance, Fig. 1 shows an example of automatic determination of the threshold value of $T = 102$ for a maximum value of $V(T)$ in (12).

However, it is difficult to differentiate dark object and dark shadow in an automatic shadow detection approach in which the threshold value is automatically determined according to the histogram distribution of the image. For example, the dark object and the dark shadow are usually in the same side of the histogram of the $(H_e + 1)/(I_e + 1)$ *ratio image* in the proposed approach. It is then hard to determine an optimal threshold using Otsu's method for the differentiation of dark object and

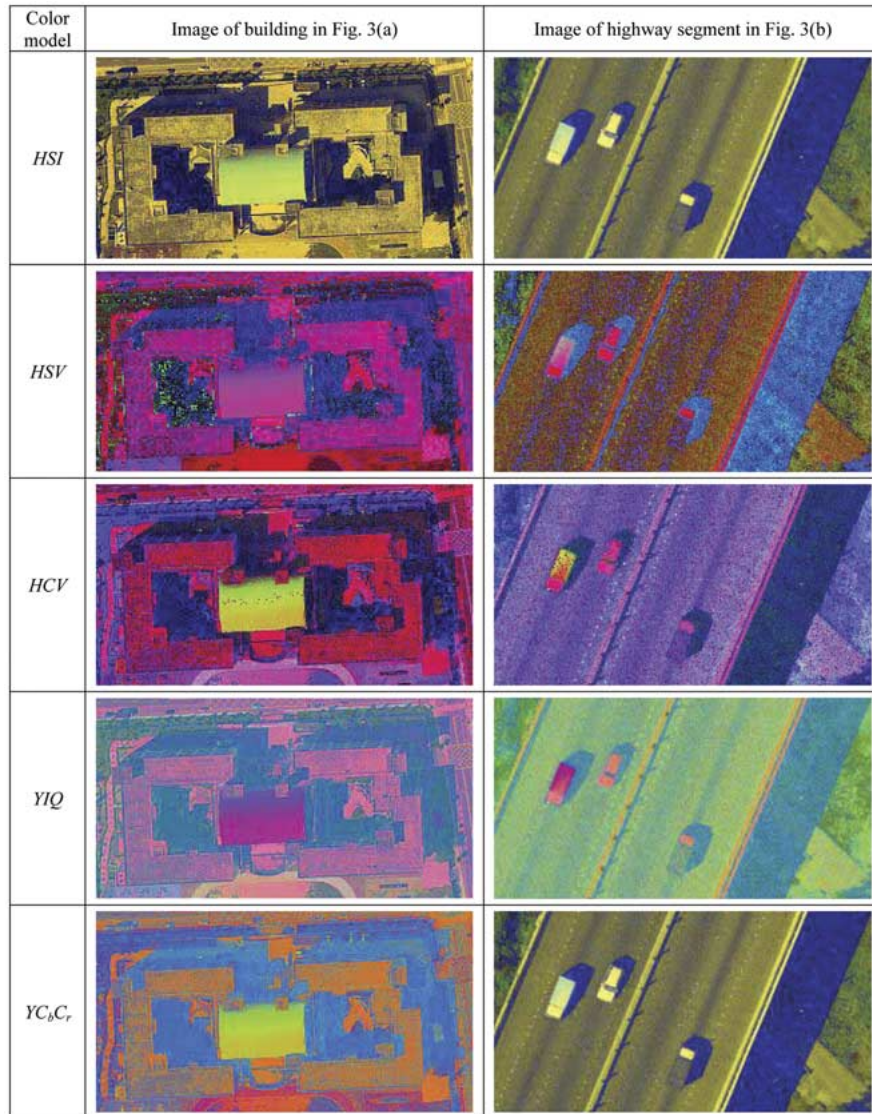


Fig. 5. Normalized composites of the color aerial images in Fig. 3 in the HSI, HSV, HCV, YIQ, and YCbCr color models (displayed in B , G , and R sequence).

dark shadow in the image. There exists a tradeoff between automation and accuracy in shadow segmentation approaches. We focus on the automation in shadow segmentation as well as preserving the shape information and compensating shadows as described in the following.

C. Shape Preservation

The shape preservation process is an option for providing additional shape information of the shadow-casting cultural features. The I_e component is used in finding the boundaries and shapes of cultural features and dark regions, including shadows in which luminance is obstructed. A Sobel operator is applied on the I_e component to obtain a gradient image, which is also scaled to have pixels' values in $[0, 255]$. The normalized gradient image is then segmented as a logical *gradient mask* by employing the Otsu's method [22], [23] in determining the gradient threshold. The *gradient mask* is further processed to obtain a *shape mask* by using a morphological CLEAN process to eliminate any isolated hole in a homogeneous area. By overlapping

the *shape mask* with the existing *shadow mask* of shadowed regions using a logical AND operator, a *shape-preserved shadow mask* was derived for use in restoring luminance of the shadowed regions. A *nonshadow mask* is also computed as the complementary of the *shape-preserved shadow mask*.

D. Shadow Compensation

Since *luminance* gives a measure of the amount of energy a sensor *perceives* from a light source, the intensity in each pixel of the RGB color aerial images is proportional to the incident *illumination (radiance)* to and the reflectance of the objects. The purpose of shadow compensation is to recover the amount of incident *illumination* of the shadowed regions to the value when not obstructed by cultural features.

This paper employs the lookup table (LUT) technique in a two-step histogram matching approach [24], band by band, for creating a final image with the *shadowed* regions been compensated. At the first step, morphological dilation operation [23] and logical AND (\cap) and NOT (\sim) operators were applied to detect connected *shadowed* regions over the *shadow mask* and

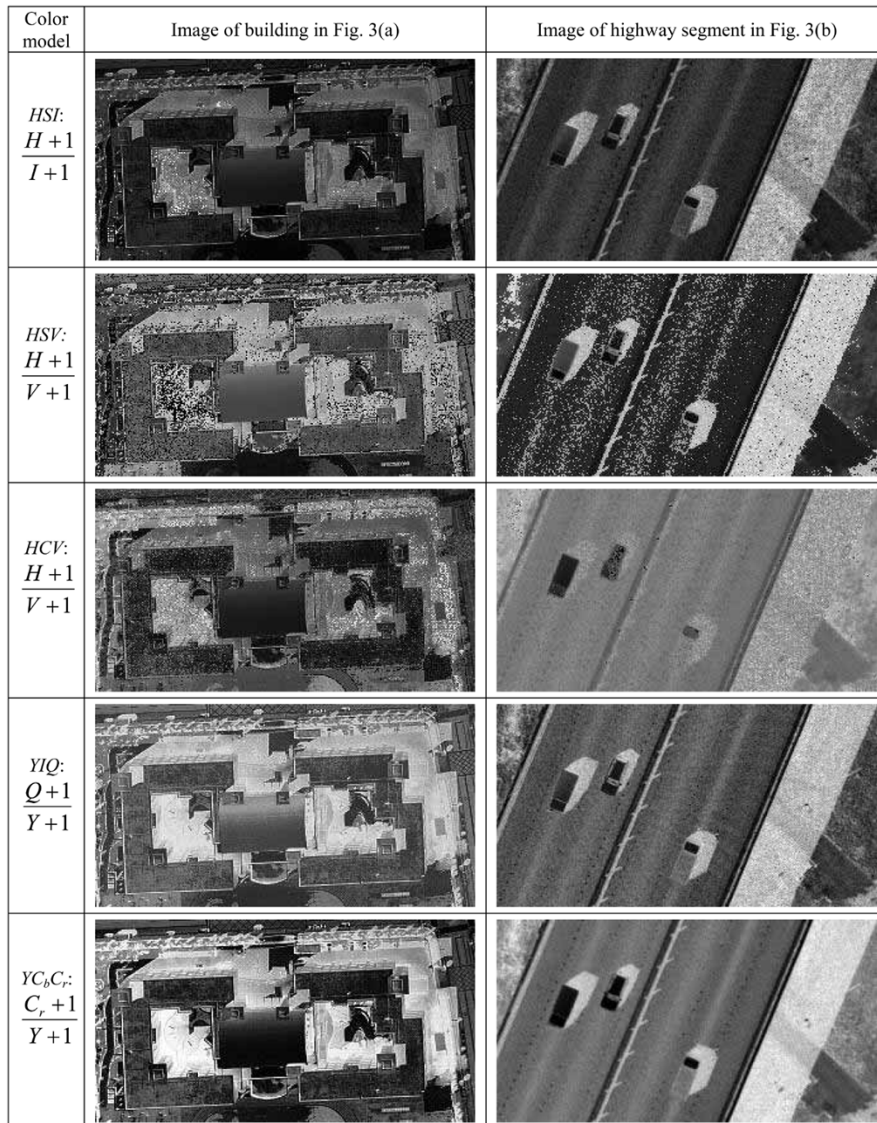


Fig. 6. Normalized $(H_e + 1)/(I_e + 1)$ ratio images of the five composites in Fig. 5.

to generate corresponding *shadow-buffer* zones of these regions. The morphological dilation, also known as Minkowski addition, of the binary *shadow mask* A by a kernel B , denoted $A \oplus B$, is defined as [23]

$$A \oplus B = \{(x, y) + (u, v) : (x, y) \in A, (u, v) \in B\} \quad (13)$$

in which the structuring elements of the kernel B determine the way of thickening of the resulting image. Starting with a nonzero pixel p in the *shadow mask* A , a connected *shadowed* region was detected by creating a sequence of sets $X_0 = \{p\}, X_1, X_2, \dots$, such that $X_n = (X_{n-1} \oplus B_{5 \times 5}) \cap A$ until $X_k = X_{k-1}$ using a 5×5 square kernel $B_{5 \times 5}$ in iterated dilation operations. The *shadow-buffer* zone of the connected *shadowed* region X_k is then generated by $Y_k = (X_k \oplus B_{10 \times 10}) \cap (\sim X_k)$ using a 10×10 square kernel $B_{10 \times 10}$ in one dilation operation. The normalized cumulated histograms of a connected *shadowed* region X_k and its *shadow-buffer* zone Y_k were used in the interpolation of output LUT grey values as schematically shown in Fig. 2. In the second step, the grey-value LUT was used to adjust the

luminance of the pixels within that connected *shadowed* region. As a result, the luminance values of pixels in each connected *shadowed* region are recovered in accordance with the pixels in local surroundings around the *shadowed* regions such that the color constancy across the shadow boundaries is observed.

IV. COMPARATIVE EVALUATIONS OF EXPERIMENTAL RESULTS

The proposed de-shadowing approach was implemented in personal computers in MATLAB programs under Microsoft Windows XP environment for removing shadows while preserving the shape information of cultured features in color aerial images. The shadow detection methods proposed in references [2] and [12] were also implemented for performance comparison and evaluation. A modified approach of [2] was also presented in this paper with normalized $I - S$ difference and the threshold K obtained by applying the Otsu's method [22], [23].

Fig. 3 shows the color aerial images of a complex building and a highway segment used in the experiment to evaluate

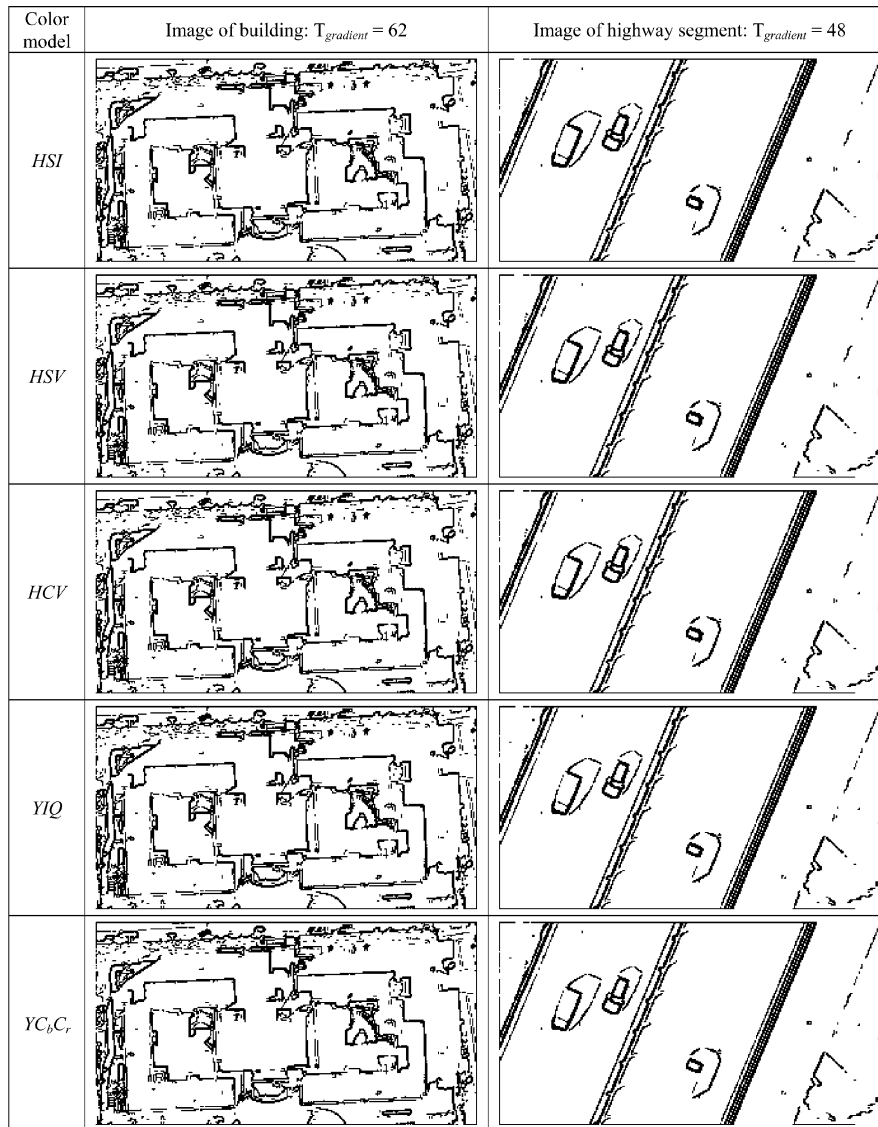


Fig. 7. Resulting *shape masks* from the I_e component of the five composites in Fig. 5.

the feasibility of the proposed procedures. The original aerial photos were taken for the purpose of 1/1000 topographic mapping in Taoyuan County, Taiwan, R.O.C., by Great Wing Airlines, Taiwan, R.O.C., using a RMK TOP 30 aerial frame camera with a photo scale of 1/5000. The aerial images were scanned from the original aerial films using a VEXCEL Ultra-Scan 5000 scanner with scanning resolution of $25 \mu\text{m}$ for use in digital photogrammetric processes. Note that the center part of the ∞ -shaped complex building in Fig. 3(a) is bluish and the right vehicle on the highway in Fig. 3(b) has almost the same hue and contrast as with the pavement. Fig. 4 shows manually interpreted *true shadow masks* as the ground truth of shadow regions for both experimental images in Fig. 3, respectively. The *true shadow masks* were used in evaluating the precision of shadow detection of the proposed approach and other methods under comparison in the experiment.

A. Visual Comparisons

Following the procedures in the proposed approach, Fig. 5 shows the normalized color composites in the HSI, HSV, HCV,

YIQ, and $YCbCr$ color models of the experimental aerial images in Fig. 3, respectively. It is observed that the shadow regions reveal blue tones in the H_e component of the five color models. Fig. 6 illustrates the scaled $(H_e + 1)/(I_e + 1)$ *ratio images* of the five color composites in Fig. 5, respectively. Note that the normalized ratio images enhance the increased *hue* property of shadow regions as expected, especially in the HSI, YIQ, and $YCbCr$ models. Fig. 7 illustrates the resulting *shape masks* of the shape preservation process in which the gradient thresholds (T_{gradient}) for the gradient images of corresponding I_e components were determined as 62 and 48 for the two experimental images, respectively. It is shown that these *shape masks* of the same experimental image are very similar due to gradient normalization although different I_e component was used in the shape preservation process.

Figs. 8 and 9 further demonstrate resulting *shape-preserved shadow masks* of the two experimental images by applying the proposed approach, the shadow detection method in [2], the modified method of [2], and the method in [12], respectively. Note that in the modified method of [2] the threshold values,

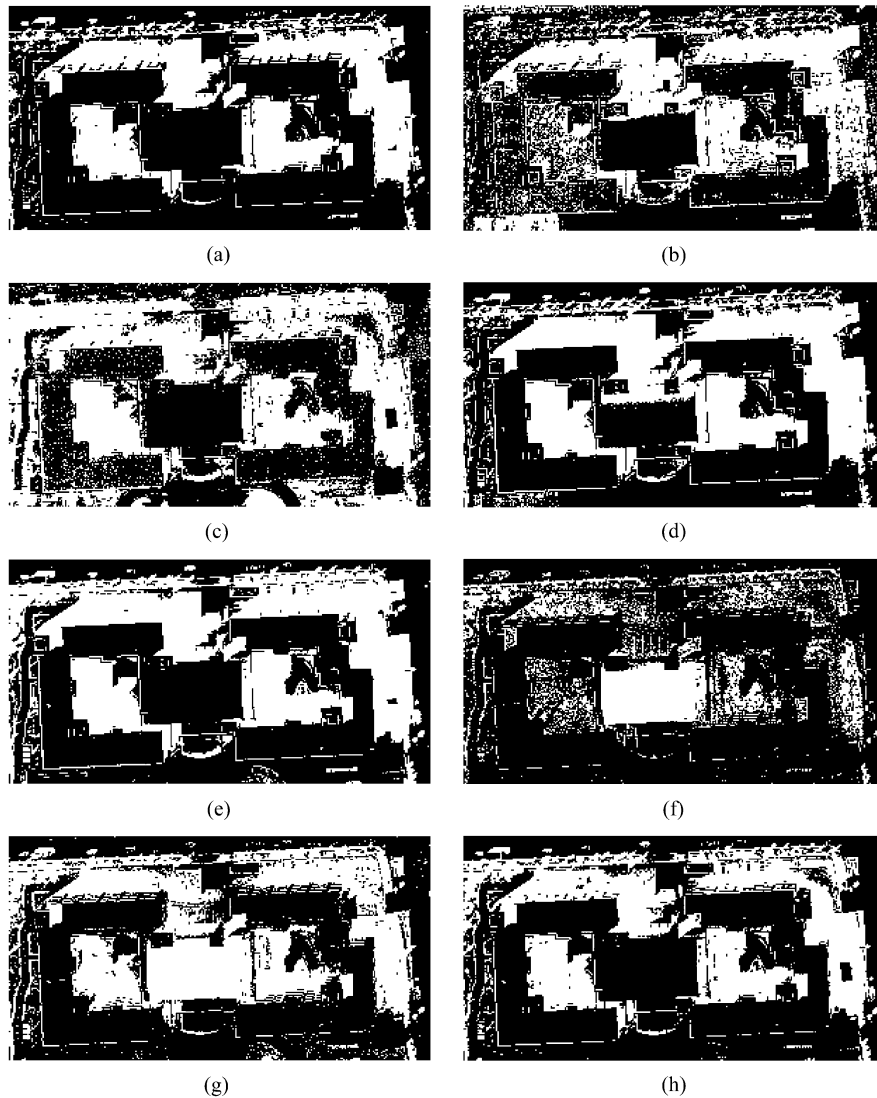


Fig. 8. Resulting *shadow masks* from the ratio images in the proposed approach and from other methods applied to Fig. 3(a). (a) HSI ($T = 66$ for ratio image), (b) HSV ($T = 107$ for ratio image), (c) HCV ($T = 86$ for ratio image), (d) YIQ ($T = 134$ for ratio image), (e) $YCbCr$ ($T = 118$ for ratio image), (f) HSI: $I - S$ [2] with $K = 0$, (g) HSI: *normalized I-S* [2] with $K = 0.51$ (Otsu's method [22], [23]), (h) HGB [12] with $T_1 = 0.1, T_2 = 80, T_3 = 80$.

i.e., $K = 0.51$ for the image in Fig. 3(a) and $K = 0.60$ for the image in Fig. 3(b), are automatically determined using the Otsu's method. Comparing detected *shadow masks* with the *true shadow mask*, it is observed that the modified method of [2] performs much better than the original method in [2] does in detecting shadows in this experiment. However, both the modified and the original methods of [2] fail to distinguish bluish objects from shadow regions as shown in Fig. 8(f) and (g). On the other hand, the threshold values, i.e., $T_1 = 0.1$ for normalized H , $T_2 = 80$ for B , and $T_3 = 80$ for $G - B$ difference for the image in Fig. 3(a) and $T_1 = 0.41$ for normalized H , $T_2 = 116$ for B , and $T_3 = 70$ for $G - B$ difference for the image in Fig. 3(b), in [12] are manually estimated with trial and error for a best shot of shadow detection of the color aerial images, respectively. As shown in Figs. 8 and 9, it is clear that the proposed approach with automatic threshold determination in the *ratio image* delivers good results in shadow detection in the HSI, YIQ, and $YCbCr$ models for both experimental images.

Figs. 10 and 11 show the RGB-based final results of shadow compensation for the two images in Fig. 3 by applying the two-step histogram matching technique. As illustrated in the results, the proposed shadow detection approach is sensitive to dark bluish areas in the HSV and YIQ models and sensitive to greenish areas in the HCV and $YCbCr$ models. For the image of the ∞ -shaped building, the resulting images in Fig. 10, except Fig. 10(f) from employing the original method in [2], dramatically improved the visualization of features within the shaded courtyards in and upper-right surroundings around the building upon de-shadowing, but resulting images of the original and modified methods of [2] illustrate distorted bright color in bluish and greenish objects due to the false detection of these objects as shadows. For the resulting image of highway segment, shadow regions of the three vehicles on the highway as well as shadow regions of the highway structure as shown in Fig. 11 were well compensated toward similar hue as

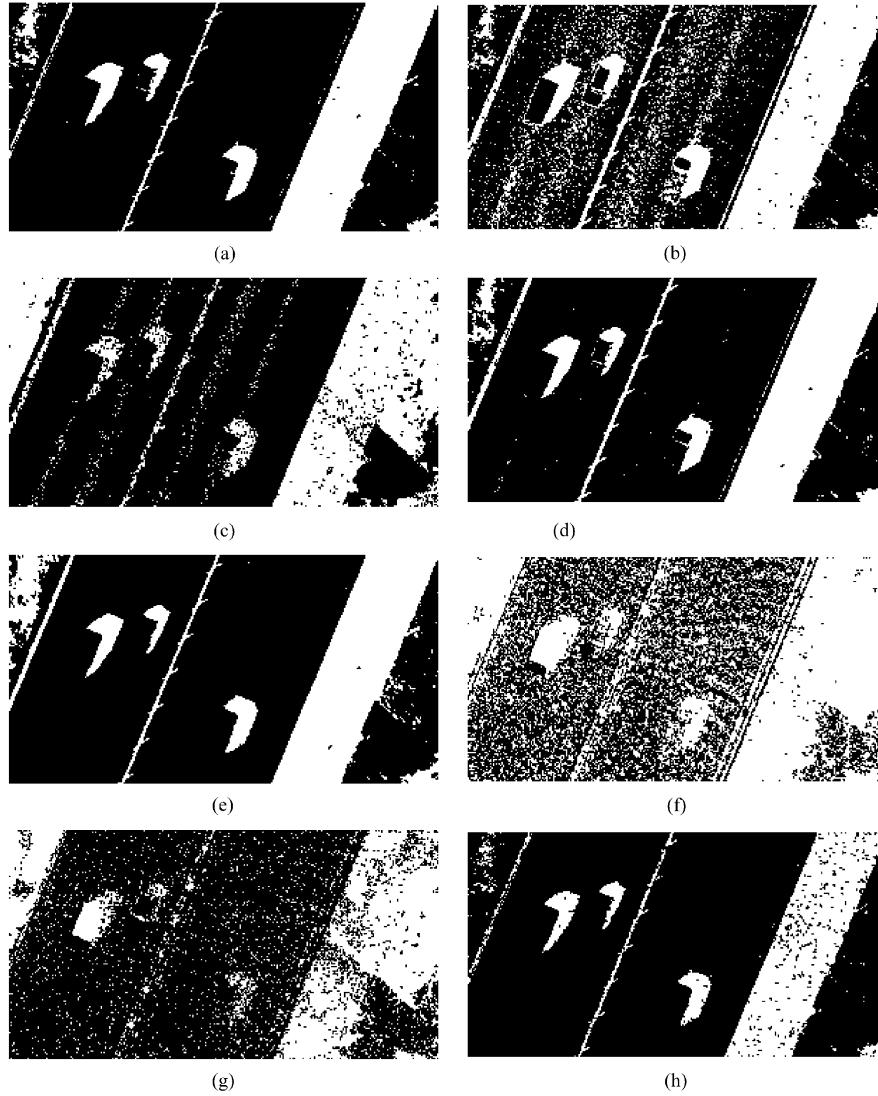


Fig. 9. Resulting *shadow masks* from the ratio images in the proposed approach and from other methods applied to Fig. 3(b). (a) HSI ($T = 102$ for ratio image). (b) HSV ($T = 111$ for ratio image). (c) HCV ($T = 136$ for ratio image). (d) YIQ ($T = 130$ for ratio image). (e) $YCbCr$ ($T = 150$ for ratio image). (f) HSI: $I-S$ [2] with $K = 0$. (g) HSI: *normalized I-S* [2] with $K = 0.60$ (Otsu's method [22], [23]). (h) HGB [12] with $T_1 = 0.41$, $T_2 = 116$, $T_3 = 70$.

the surrounding neighborhood in the results of applying the proposed approach in the HSI, YIQ, and $YCbCr$ models.

It is concluded that the proposed approach enhances the spectral intensities of the pixels within the *shadowed* regions to reveal a wealth of new details that were not discerned in the original images.

B. Shadow Detection Accuracy Assessment

Following the concept of *error matrix* [1], [3] and the terminology in references [25] and [26], we define the evaluation metrics of shadow detection accuracy assessment at the pixel level as follows.

- 1) Producer's accuracies:

(a) shadow:

$$\eta_s = \frac{TP}{TP + FN} \quad (14)$$

(b) nonshadow:

$$\eta_n = \frac{TN}{FP + TN}. \quad (15)$$

- 2) User's accuracies:

(a) shadow:

$$ps = \frac{TP}{TP + FP} \quad (16)$$

(b) nonshadow:

$$pn = \frac{TN}{TN + FN}. \quad (17)$$

- 3) Overall accuracy:

$$\tau = \frac{TP + TN}{TP + TN + FP + FN} \quad (18)$$

in which TP (*true positive*) is the number of shadow pixels correctly identified, FN (*false negative*) is the number of shadow pixels identified as nonshadows,

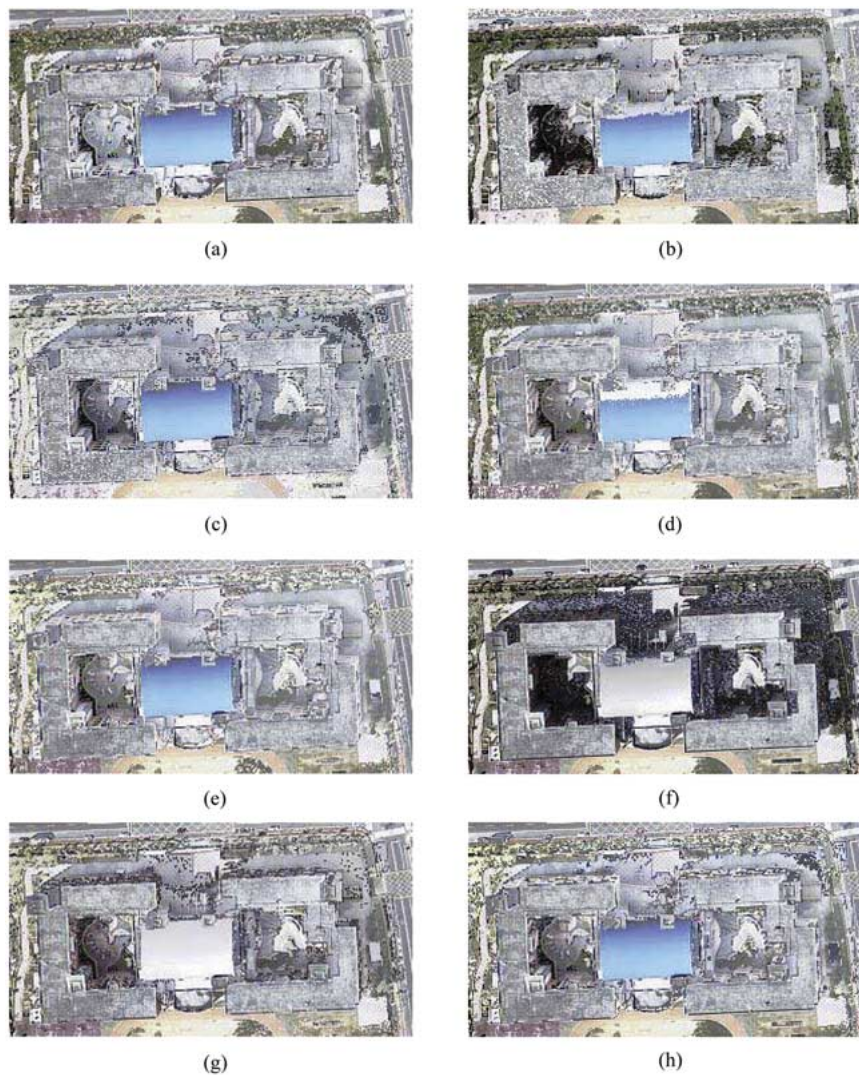


Fig. 10. Final results of shadow compensation on the image of building in Fig. 3(a) from applying the proposed approach and other methods. (a) HSI. (b) HSV. (c) HCV. (d) YIQ. (e) $YCbCr$. (f) HSI: $I - S$ [2] with $K = 0$. (g) HSI: *normalized I-S* [2] with $K = 0.51$ (Otsu's method [22], [23]). (h) HGB [12] with $T_1 = 0.1, T_2 = 80, T_3 = 80$.

FP (*false positive*) is the number of nonshadow pixels identified as shadows, TN (*true negative*) is the number of nonshadow pixels correctly identified, and $TP + TN + FP + FN$ stands for the total number of pixels in the image.

Among these metrics, the producer's accuracies are measures of the *correctness* [26] of the algorithm and indicate how well pixels of known categories are correctly classified. The user's accuracies are measures of the *precision* [25] of the algorithm and indicate the probabilities of pixels been correctly classified into actual categories on the ground. The overall accuracy is a measure of relative effectiveness of the algorithm and reports the *percentage correct* [3] or the closeness of the estimate to the true value. These metrics together demonstrate the significance of a shadow detection algorithm. For a good algorithm, values of these evaluation metrics should be high.

Experimental results of shadow detection accuracy measurements of the proposed automatic approach as well as

the methods in references [2] and [12] are summarized in Tables I and II by evaluating resulting *shadow masks* in Figs. 8 and 9 with respect to the *true shadow masks* of Fig. 3(a) and (b), respectively. It is shown that the HSI model is the optimal choice for the proposed automatic approach as with the highest user's accuracy in shadow (p_s) and overall accuracy (τ) in the experiments. The YIQ and $YCbCr$ models are also excellent for the proposed automatic approach with high values in shadow detection rate (η_s) and overall accuracy (τ) although they are sensitive to bluish and greenish objects. The accuracy metrics also illustrate that the proposed automatic approach applied in the HSI, YIQ, and $YCbCr$ models is clearly better than those proposed in references [2] and [12], which requires manual estimates of several thresholds that are scene dependent.

V. CONCLUSION

This paper exploits the properties of cast shadows in luminance and chromaticity and implements fundamental chromatic

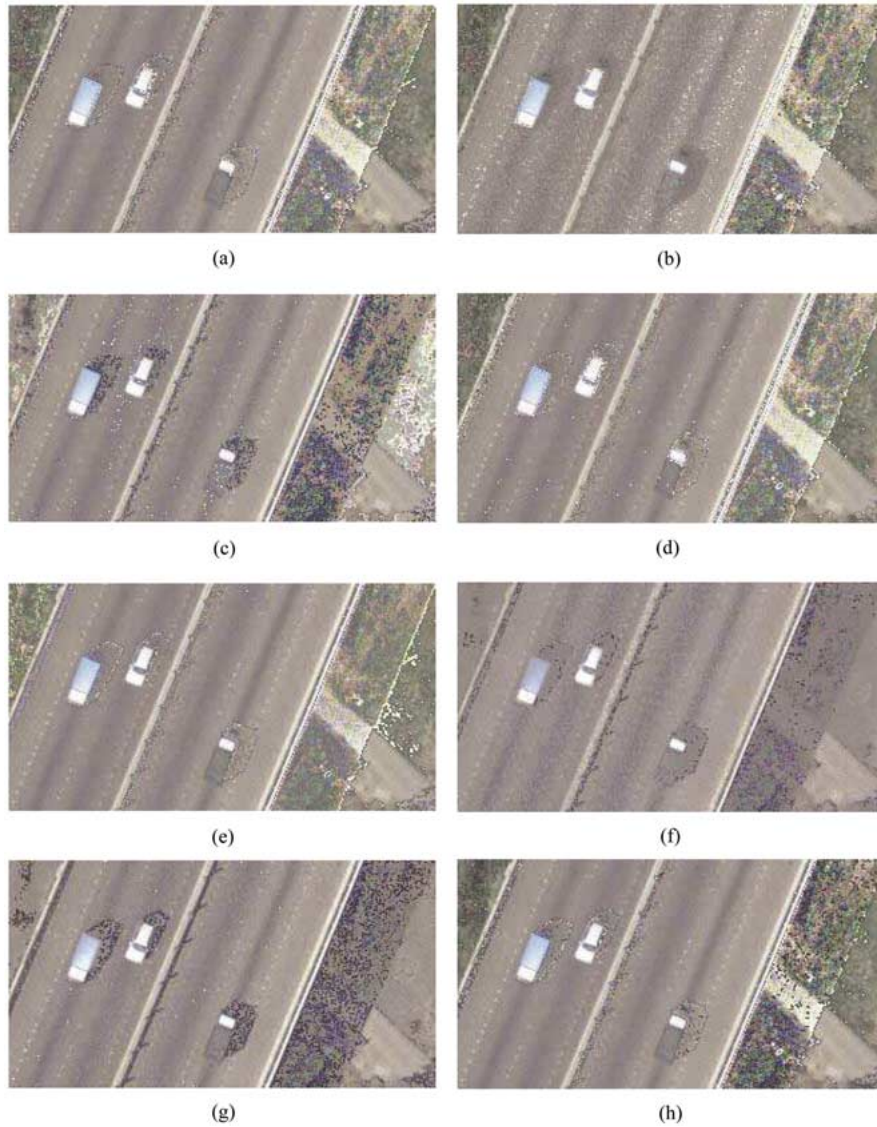


Fig. 11. Final results of shadow compensation of the image of highway segment in Fig. 3(b) from applying the proposed approach and other methods. (a) HSI. (b) HSV. (c) HCV. (d) YIQ. (e) $YCbCr$. (f) HSI: $I - S$ [2] with $K = 0$. (g) HSI: *normalized I-S* [2] with $K = 0.60$ (Otsu's method [22], [23]). (h) HGB [12] with $T_1 = 0.41, T_2 = 116, T_3 = 70$.

TABLE I
SHADOW DETECTION ACCURACY MEASUREMENTS OF THE IMAGE IN Fig. 3(a)

| Method | Color Model | Producer's accuracies | | User's accuracies | | Overall accuracy τ (%) |
|---------------------------|-------------|------------------------|---------------------------|---------------------|------------------------|--------------------------------|
| | | Shadow η_s (%) | Nonshadow η_n (%) | Shadow p_s (%) | Nonshadow p_n (%) | |
| Proposed | HSI | 89.9 | 99.0 | 97.9 | 94.7 | 95.7 |
| | HSV | 79.6 | 86.6 | 76.5 | 88.6 | 84.1 |
| | HCV | 88.8 | 78.3 | 69.1 | 92.7 | 82.0 |
| | YIQ | 95.6 | 94.4 | 90.3 | 97.5 | 94.8 |
| | $YCbCr$ | 97.5 | 93.2 | 88.7 | 98.6 | 94.7 |
| [2] ¹ | HSI | 39.5 | 88.5 | 65.3 | 72.8 | 71.2 |
| Modified [2] ² | HSI | 79.2 | 85.1 | 74.4 | 88.2 | 83.0 |
| [12] ³ | HGB | 88.1 | 96.6 | 93.5 | 93.7 | 93.6 |

Notes: 1. Threshold: $K=0$ for $I-S$ difference.

2. Threshold: $K=0.51$ (Otsu's method [22][23]) for normalized $I-S$ difference.

3. Thresholds: $T_1=0.10$ for normalized H , $T_2 = 80$ for B , and $T_3=80$ for $G-B$ difference.

TABLE II
SHADOW DETECTION ACCURACY MEASUREMENTS OF THE IMAGE IN FIG. 3(b)

| Method | Color Model | Producer's accuracies | | User's accuracies | | Overall accuracy τ (%) |
|---------------------------|-------------|------------------------|---------------------------|---------------------|------------------------|--------------------------------|
| | | Shadow η_s (%) | Nonshadow η_n (%) | Shadow p_s (%) | Nonshadow p_n (%) | |
| Proposed | HSI | 88.2 | 99.3 | 97.4 | 96.4 | 96.6 |
| | HSV | 93.3 | 87.8 | 70.8 | 97.6 | 89.1 |
| | HCV | 81.5 | 88.0 | 68.3 | 93.7 | 86.4 |
| | YIQ | 92.2 | 98.8 | 96.2 | 97.6 | 97.2 |
| | $YCbCr$ | 91.2 | 97.5 | 92.1 | 97.2 | 96.0 |
| [2] ¹ | HSI | 87.9 | 56.0 | 38.9 | 93.6 | 63.7 |
| Modified [2] ² | HSI | 62.8 | 82.0 | 52.6 | 87.4 | 77.4 |
| [12] ³ | HGB | 79.1 | 99.7 | 98.8 | 93.7 | 94.7 |

Notes: 1. Threshold: $K=0$ for $I-S$ difference.

2. Threshold: $K=0.60$ (Otsu's method [22][23]) for normalized $I-S$ difference.

3. Thresholds: $T_1=0.41$ for normalized H , $T_2 = 116$ for B , and $T_3=70$ for $G-B$ difference.

thresholding processes under physical model in an automatic de-shadowing approach for shadow compensation in color aerial images. The proposed approach employs *spectral ratioing* and automatic thresholding techniques in detecting shadow regions, thus effectively eliminating the requirement of *a priori* geometric knowledge or information about the scene and the source of illumination. Meanwhile, the proposed approach also implements a two-step histogram matching technique to compensate shadow regions from their surrounding neighborhoods. Experimental results from applying the proposed approach in de-shadowing the color aerial images of a complex building and a highway segment in five invariant color spaces were evaluated and compared with the results from applying other methods in terms of visual comparisons and shadow detection accuracy assessment. It is proved that the proposed approach not only automatically detects shadow regions with high precision but also compensates the luminance of shadow regions toward that of direct illumination in complex urban environment. Our conclusion is that applying the proposed de-shadowing approach in the HSI, YIQ and $YCbCr$ color models will produce images with dramatically improved visualization of features within recovered shadow regions. Moreover, the preserved shape information of shadow regions and cultured features provides important geometric and semantic evidences for a high performance system of 3-D building extraction and model reconstruction in complex urban environment using color aerial images.

REFERENCES

- [1] T. M. Lillesand and R. W. Kiefer, *Remote Sensing and Image Interpretation*, 4th ed. New York: Wiley, 2000.
- [2] A. M. Polidoro, F. C. Flores, N. N. Imai, A. M. G. Tommaselli, and C. Franco, "Automatic shadow segmentation in aerial color images," in *Proc. XVI Brazilian Symp. Computer Graphics and Image Processing*, Oct. 12–15, 2003, pp. 270–277.
- [3] *Manual of Photographic Interpretation*, 2nd ed. Bethesda, MD: American Society Photogrammetry and remote sensing (ASPRS), 1997.
- [4] A. Huertas and R. Nevatia, "Detecting buildings in aerial images," *Comput. Vis. Graph. Image Process.*, vol. 41, pp. 131–152, 1988.
- [5] M. Nagao, T. Matsuyama, and Y. Ikeda, "Region extraction and shape analysis in aerial images," *Comput. Graph. Image Process.*, vol. 10, no. 3, pp. 195–223, Jul. 1979.
- [6] R. B. Irvin and D. M. McKeown Jr., "Methods for exploiting the relationship between buildings and their shadows in aerial imagery," *IEEE Trans. Syst., Man, Cybern.*, vol. 19, no. 6, pp. 1564–1575, Dec. 1989.
- [7] Y. Liow and T. Pavlidis, "Use of shadows for extracting buildings in aerial images," *Comput. Vis. Graph. Image Process.*, vol. 49, pp. 242–277, 1990.
- [8] J. M. Scanlan, D. M. Chabries, and R. W. Christiansen, "A shadow detection and removal algorithm for 2-D images," in *Proc. Int. Conf. Acoustics, Speech, and Signal Processing*, vol. 4, 1990, pp. 2057–2060.
- [9] V. J. D. Tsai, "Automatic shadow detection and radiometric restoration on digital aerial images," in *Proc. IGARSS*, Toulouse, France, Jul. 21–25, 2003, pp. 732–733.
- [10] S. Watanabe, K. Miyajima, and N. Mukawa, "Detecting changes of buildings from aerial images using shadow and shading model," in *Proc. 14th Int. Conf. Pattern Recognition*, vol. 2, 1998, pp. 1408–1412.
- [11] A. Susuki, A. Shio, H. Arai, and S. Ohtsuka, "Dynamic shadow compensation of aerial images based on color and spatial analysis," in *Proc. 15th Int. Conf. Pattern Recognition*, Barcelona, Catalonia, Spain, Sep. 3–7, 2000, pp. 317–320.
- [12] J. Huang, W. Xie, and L. Tang, "Detection of and compensation for shadows in colored urban aerial images," in *Proc. 5th World Congr. Intelligent Control and Automation*, Hangzhou, China, Jun. 15–19, 2004, pp. 3098–3100.
- [13] B. T. Phong, "Illumination for computer generated pictures," *Commun. ACM*, vol. 18, no. 6, pp. 311–317, 1975.
- [14] R. C. Gonzalez and R. E. Woods, *Digital Image Processing*. Reading, MA: Addison-Wesley, 1992.
- [15] W. K. Pratt, *Digital Image Processing*, 2nd ed. New York: Wiley, 1991.
- [16] A. R. Smith, "Color gamut transform pairs," in *Proc. SIGGRAPH*, vol. 3(ACM), Atlanta, GA, Aug. 23–25, 1978, pp. 12–19.
- [17] H. J. Smith, "Putting colors in order," *Dr. Dobbs's J.*, vol. 1993, p. 40, Jul. 1993.
- [18] F. J. Bingley, "Color vision and colorimetry," in *Television Engineering Handbook*, D. G. Fink, Ed. New York: McGraw-Hill, 1957.
- [19] M.-J. Chen, M.-C. Chi, C.-T. Hsu, and J.-W. Chen, "ROI video coding based on H2.63+ with robust skin-color detection technique," in *Proc. IEEE Conf. Consumer Electronics*, Jun. 17–19, 2003, pp. 44–45.
- [20] P. Kumar, K. Sengupta, and A. Lee, "A comparative study of different color spaces for foreground and shadow detection for traffic monitoring system," in *Proc. IEEE 5th Int. Conf. Intelligent Transportation Systems*, Singapore, Sep. 2–6, 2002, pp. 100–105.
- [21] S. M. Adler-Golden, M. W. Matthew, G. P. Anderson, G. W. Felde, and J. A. Gardner, "An algorithm for de-shadowing spectral imagery," in *Proc. AVIRIS Earth Sciences and Applications Workshop*, 2000, p. 8.
- [22] N. Otsu, "A threshold selection method from gray level histograms," *IEEE Trans. Syst., Man, Cybern.*, vol. SMC-9, no. 1, pp. 62–69, Mar. 1979.
- [23] A. McAndrew, *Introduction to Digital Image Processing with MATLAB*. Boston, MA: Course Technology, 2004.
- [24] V. J. D. Tsai and Y. T. Huang, "Automated image mosaicking," *J. Chin. Inst. Eng.*, vol. 28, no. 2, pp. 329–340, 2005.
- [25] A. Prati, I. Mikic, M. M. Trivedi, and R. Cucchiara, "Detecting moving shadows: Algorithms and evaluations," *IEEE Trans. Pattern Anal. Mach. Intell.*, vol. 25, no. 7, pp. 918–923, Jul. 2003.
- [26] J. Yao and Z. Zhang, "Systematic static shadow detection," in *Proc. 17th Int. Conf. Pattern Recognition*, vol. 2, 2004, pp. 76–79.



Victor J. D. Tsai received the B.S. and M.S. degrees in civil engineering from the National Chung Hsing University, Taiwan, R.O.C., in 1981 and 1987, respectively, and the Ph.D. degree in civil and environmental engineering from the University of Wisconsin, Madison, in 1994.

He has been with the Department of Civil Engineering, National Chung Hsing University, since 1984, where he has been an Associate Professor since 1995. His research interests focus on automation of digital photogrammetric processes, remote sensing and image processing, and techniques in geographic information systems.